Synchronous Voltage Reconstruction of VSC-HVDC Systems Under Weak Grid Conditions

Weiye Diao, *Student Member*, *IEEE*, Ao Liu, Jun Mei, *Member*, *IEEE*, Linyuan Wang, Guanghua Wang, and Fujin Deng, *Senior Member*, *IEEE*

***Abstract*—Under weak grid conditions, grid impedance is coupled with a control system for voltage source converter based high-voltage direct current (VSC-HVDC) systems, resulting in decreased synchronization stability. Unfortunately, most studies are based on the assumption that impedance ratio (*R*/*X*) is sufficiently small to ignore the effects of grid impedance. In this study, we establish a dynamic coupling model that includes grid impedance and control loops, revealing the influence mechanism of *R*/*X* on synchronization stability from a physical perspective. We also quantify the stability range of *R*/*X* in the static analysis model and introduce a sensitivity factor to measure its effect on voltage stability. Additionally, we utilize a dynamic analysis model to evaluate power angle convergence, proposing a corresponding stability criterion. We then present a method of synchronous voltage reconstruction aimed at enhancing the grid strength. Theoretical analysis shows that this method can effectively mitigate the effects of coupling between grid impedance and the controller under weak grid conditions, ensuring stable operation even under extremely weak grid conditions. Experiments validate the accuracy and effectiveness of the analysis and method.**

***Index Terms*—Synchronous voltage reconstruction, impedance ratio (*R*/*X*), grid impedance, weak grid, coupling model, voltage source converter based high-voltage direct current (VSC-HVDC), grid-following control, short-circuit ratio (SCR).**

I. INTRODUCTION

VOLTAGE source converter based high-voltage direct current (VSC-HVDC) systems have been designed for renewable energy integration and transmission. These systems are used, for example, to evacuate electrical power from offshore wind farms, connect energy centers and load centers over long distances, and provide electricity to remote mountainous regions and islands [1], [2]. However, long-distance transmission lines and the presence of numerous transformers result in a high-impedance grid. In addition, the high proportion of renewable energy and power electronic devices connected to the AC grid reduces grid strength, leading to weak grid characteristics [3].

Currently, VSC-HVDC systems primarily use grid-following (GFL) control based on phase-locked loop (PLL) synchronization [4]. For simplicity, the GFL-VSC refers to the GFL-based VSC-HVDC used in this study. Recent reports from various national power grids indicate an increasing risk of instability due to the loss of synchronism by GFL-VSC systems under weak grid conditions [5], [6]. Cases include the Estlink project between Estonia and Finland, the Caprivi Link project in Namibia, and the back-to-back VSC project in Chongqing and Hubei, China. GFL-VSCs are widely used in different scenarios, with significant differences in the line impedance characteristics at various voltage levels. In addition to the magnitude of impedance or short-circuit ratio (SCR), the phase of impedance, referred to as the impedance ratio (*R*/*X*), also significantly affects synchronization stability [7].

Adding auxiliary circuits or devices, such as static synchronous compensator (STATCOM), between high-voltage direct current (HVDC) terminals and the grid is effective for enhancing synchronization stability in weak grids [8]. However, this approach is limited by geographical constraints and requires additional investments. In addition, the effectiveness of reactive power injection in improving synchronization stability is closely related to *R*/*X* [9]. Therefore, enhancing the adaptability of the converter to weak grids and varying *R*/*X* are pressing issues that must be addressed.

Some researchers have proposed using the power balance as the synchronization mechanism for converters, achieving grid synchronization by autonomously constructing the voltage and phase angle without PLLs. This technology is known as grid-forming (GFM) control [4]. The BorWin6 offshore wind power VSC-HVDC project in Germany, scheduled for commissioning in 2027, plans to employ this technology [10]. However, studies [11], [12] have found that although GFM control techniques such as virtual synchronous generator (VSG), power synchronization control (PSC), and matching control can enhance synchronization stability, they may also introduce issues such as angle oscillations and slow dynamic response. Worse, the GFM control has limited fault current suppression during large disturbances, necessitating a switch to the GFL control to achieve current limit-

---

Manuscript received: June 20, 2024; revised: September 26, 2024; accepted: November 20, 2024. Date of CrossCheck: November 20, 2024. Date of online publication: April 30, 2025.

This work was supported in part by the National Natural Science Foundation of China (No. 52077037) and in part by the Science and Technology Projects of Jiangsu Province (No. BE2022016).

W. Diao, A. Liu, J. Mei (corresponding author), L. Wang, G. Wang, and F. Deng are with the School of Electrical Engineering, Southeast University, Nanjing 210096, China (e-mail: Domiye@seu. edu. cn; 220222805@seu. edu. cn; mei_jun@seu.edu.cn; 220222687@seu.edu.cn; meihua@seu.edu.cn; fdeng@seu.edu.cn.).

DOI: 10.35833/MPCE.2024.000650

JOURNAL OF MODERN POWER SYSTEMS AND CLEAN ENERGY

ing [13]. This poses significant challenges to the stable operation of VSCs in weak grids. Therefore, if the synchronization stability issue of converters in weak grids can be resolved, GFL control may still be considered a simpler solution for grid-connected converters. Current research has primarily focused on two aspects: stability [14]-[17] and control [18]-[25].

In terms of stability mechanisms, [14] and [15] investigated how PLL affects small-signal stability in high-voltage direct current (HVDC) systems when connected to an AC grid. An inverter impedance model was previously developed considering the PLL influence, utilizing the generalized Nyquist criterion to assess system stability and analyzing the critical factors that affect stability [16], [17]. Nonetheless, the direct measurement of the *dq* axis impedance is challenging, and its physical interpretation remains unclear. Most current research has focused on the interaction between SCR and PLL, placing less emphasis on *R*/*X*. The study in [7] indicated that *R*/*X* is closely related to synchronization stability, particularly in a weak grid, where ignoring the role of *R*/*X* in practical applications is risky. However, the existing work has not provided an effective stabilization method.

Significant progress has been made in synchronization stability control, with a primary focus on enhancing current loops and modifying PLLs. The studies in [18] - [20] improved the filtered resonance and current loop, thus enhancing the stability margin of the system. However, this method introduces an auxiliary control loop that is highly sensitive to parameter variations and steady-state operating conditions. In addition, it fails to consider the PLL. As a result, [21] and [22] applied dynamic compensation to the PLL inner loop and proposed a voltage feedforward as a viable approach to vector control. The PLL parameters and structure were optimized to enhance performance under weak grid conditions [23], [24]. In [25], a compensation for the PLL angle based on the estimated or measured grid impedance was proposed. However, the method of transforming the PLL involves reshaping the impedance for converters, which may affect the dynamic performance or have limited applicability.

Virtual impedance is a commonly used approach to address synchronization stability issues. The study in [20] proposed a feedforward virtual inductance control strategy that integrates the feedforward virtual inductance into the current control loop of grid-connected converters, thereby ensuring stable operation under weak grid conditions. The studies in [26] and [27] proposed a dynamic virtual impedance control method that adjusts virtual impedance in real time to improve the dynamic performance and stability of GFL inverters under weak grid conditions. However, the speed of these adjustments is limited, and system stability may be compromised during significant fluctuations in grid frequency and voltage. Notably, these virtual impedance methods typically enhance the SCR by altering the magnitude of line impedance, effectively strengthening the grid. However, they do not consider the effects of *R*/*X* and stability boundaries, nor do they adjust the phase of *R*/*X*.

As noted, little research has been conducted on the synchronization stability of *R*/*X* in GFL-VSC systems under weak grid conditions. This study addresses this gap by analyzing the instability mechanisms related to *R*/*X* in weak grids and proposing a synchronous voltage reconstruction method, which effectively modifies grid impedance to enhance synchronization stability. The main contributions of this study are summarized as follows.

1) A small-signal model for synchronization stability of the GFL-VSC is established, which effectively captures the dynamic coupling process among the SCR, *R*/*X*, current control loop, and PLL.

2) The effect mechanism of *R*/*X* on the voltage and power angle stability is investigated to quantify the stability range of *R*/*X* and provide corresponding stability criteria.

3) A novel synchronous voltage reconstruction method is proposed, which enhances synchronization stability across various grid strengths and impedance characteristics while maintaining existing control schemes.

The remainder of this paper is organized as follows. Section II establishes a small-signal model for synchronization stability of the GFL-VSC. Section III discusses the effect mechanism of *R*/*X* on the synchronization stability of the GFL-VSC. Section IV proposes a synchronous voltage reconstruction method based on the grid impedance information. Experimental results verify the effectiveness of the analysis and method presented in Section V. Section VI concludes the paper.

II. SMALL-SIGNAL MODEL FOR SYNCHRONIZATION STABILITY OF GFL-VSC

Figure 1 shows the topology and control block of a VSC-HVDC system connected to a weak grid using an L-type filter and impedance. L_f and R_f are the filter inductance and parasitic resistance, respectively. L_g and R_g are the inductance and resistance of the grid, respectively. $Z_g = R_g + \mathrm{j}L_g$ is the total impedance of the grid, which can be obtained from the impedance estimation. Unless otherwise specified, all electrical variables in this study are expressed in per-unit values. $\dot{U}_o$ is the VSC output voltage. $\dot{U}_t$ and $\dot{U}_g$ are the voltage at the point of common coupling (PCC) and grid voltage, respectively. $\dot{I}_{abc}$ is the grid-connected current. u_{dc} is the voltage at the DC side.

A more detailed high-order model is established for the synchronization stability of the GFL-VSC. This model considers the dynamic coupling process among the SCR, *R*/*X*, current control loop, and PLL, thereby enhancing the comprehensiveness of the analysis.

A. Typical Small-signal Model for Synchronization Stability of GFL-VSC

According to Fig. 1, the *q*-axis component of $\dot{U}_t$ can be derived as:

$$u_{tq} = U_g \sin(\delta_g - \delta_c) + R_g i_q + \frac{L_g}{\omega_0}\frac{\mathrm{d}i_q}{\mathrm{d}t} + \frac{\omega_c}{\omega_0} L_g i_d \tag{1}$$

where δ_g is the phase angle of $\dot{U}_g$; i_d and i_q are the *d*- and *q*-axis currents, respectively; ω_0 is the grid frequency; and δ_c and ω_c are the phase angle and frequency of the PLL, respectively.

The PLL obtains the phase angle used for the *dq* frame transformation by controlling u_{tq}. This can be described as:

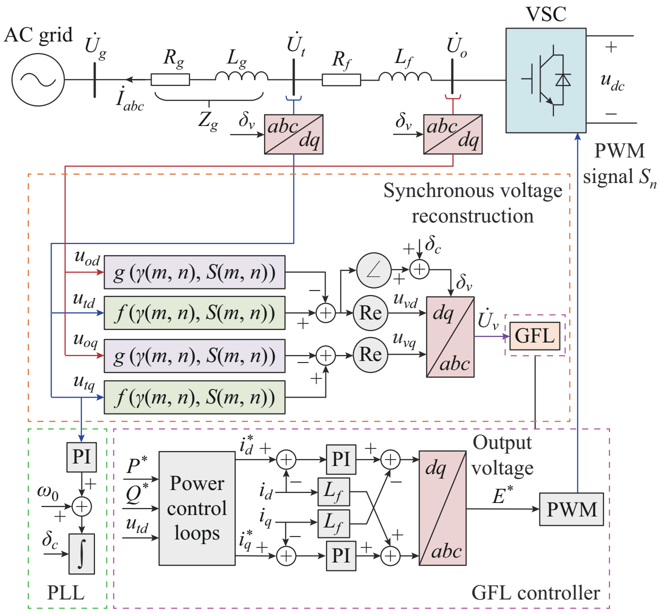

Fig. 1. Topology and control block of a VSC-HVDC system connected to a weak grid.

$$\delta_c = \frac{\omega_c}{s} = \frac{1}{s} G_{pll}(s) u_{tq} \tag{2}$$

where $G_{pll}(s) = k_{p,pll} + k_{i,pll}/s$ is the transfer function of the proportional-integral (PI) controller in the PLL, and $k_{p,pll}$ and $k_{i,pll}$ are the proportional and integral parameters, respectively. When the PLL operates successfully, $\omega_c = \omega_0$. Linearizing (1) at the equilibrium point yields:

$$\Delta u_{tq} = -U_g \cos(\delta_0)\Delta\delta_c + \underbrace{\left(\frac{L_g}{\omega_0}s + R_g\right)\Delta i_q + L_g \Delta i_d}_{\Delta u_{zq}} \tag{3}$$

where $\delta_0 = \arcsin((R_g i_q^* + L_g i_d^*)/U_g)$, and the superscript $*$ denotes the rated value; and Δu_{zq} is a small disturbance component of the impedance voltage.

However, the typical small-signal model for synchronization stability of the GFL-VSC shown in Fig. 2 fails to accurately depict the influence of the current control loop and R/X on the dynamic characteristics of the PLL. In fact, $\dot{I}_{abc}$ directly affects the dynamic changes in $\dot{U}_t$ by impedance, which in turn causes dynamic adjustments of the PLL and current control loop. This leads to a change in $\dot{I}_{abc}$ and eventually affects $\dot{U}_t$. The interactions among $\dot{U}_t$, impedance, PLL, and current control loop form a complex process. Therefore, it is neccessary to establish a small-signal model for synchronization stability that can describe these dynamic coupling processes is necessary.

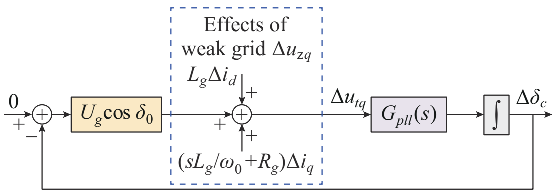

Fig. 2. Typical small-signal model for synchronization stability of GFL-VSC.

B. Small-signal Model for Synchronization Stability of GFL-VSC with Dynamic Coupling

Based on Fig. 1, the small-signal expressions of $\dot{U}_o$ in the dq frame and the current loop can be easily obtained by:

$$\begin{cases} \Delta e_d = \left(\dfrac{L}{\omega_0}s + R\right)\Delta i_d - L\Delta i_q - (U_g \sin\delta_0)\Delta\delta_c \\ \Delta e_q = \left(\dfrac{L}{\omega_0}s + R\right)\Delta i_q + L\Delta i_d - (U_g \cos\delta_0)\Delta\delta_c \end{cases} \tag{4}$$

$$\begin{cases} \Delta e_d = -(k_{p,c} + k_{i,c}/s)\Delta i_d - L_f \Delta i_q \\ \Delta e_q = -(k_{p,c} + k_{i,c}/s)\Delta i_q + L_f \Delta i_d \end{cases} \tag{5}$$

where $L = L_f + L_g$; $R = R_f + R_g$; and $k_{p,c}$ and $k_{i,c}$ are the proportional and integral parameters of the PI controller in the current control loop, respectively. Combining (4) and (5), the small-signal expression for the VSC output current can be obtained as:

$$\begin{cases} \Delta i_d = \dfrac{L_g U_g \cos\delta_0 + G_1(s) U_g \sin\delta_0}{G_1^2(s) + L_g^2}\Delta\delta_c \\ \Delta i_q = \dfrac{G_1(s) U_g \cos\delta_0 - L_g U_g \sin\delta_0}{G_1^2(s) + L_g^2}\Delta\delta_c \end{cases} \tag{6}$$

where $G_1(s) = Ls/\omega_0 + R + k_{p,c} + k_{i,c}/s$. In addition, R/X and SCR value are defined as $\gamma = R_g/L_g$ and $SCR = 1/Z_g$, respectively. Thus, the expression reflecting the dynamic coupling process of the system in a weak grid can be written as:

$$\Delta u_{zq} = (G_2(s)G_4(s) + G_3(s)G_5(s))\Delta\delta_c \tag{7}$$

$$\begin{cases} G_2(s) = \dfrac{L_g U_g \cos\theta_0 + G_1(s) U_g \sin\delta_0}{G_1^2(s) + L_g^2} \\ G_3(s) = \dfrac{G_1(s) U_g \cos\theta_0 - L_g U_g \sin\delta_0}{G_1^2(s) + L_g^2} \\ G_4(s) = \dfrac{1}{SCR \cdot \sqrt{1+\gamma^2}} \\ G_5(s) = \dfrac{s + \omega_0^2 \gamma}{\omega_0 \cdot SCR \cdot \sqrt{1+\gamma^2}} \end{cases} \tag{8}$$

Both SCR and R/X clearly affect the current dynamic characteristics. This influence is then transmitted through Δu_{zq} to directly affect Δu_{tq}, which in turn affects the stability of $\Delta\delta_c$. Therefore, it is inaccurate to consider only SCR while ignoring R/X.

When (2)-(9) are combined, the proposed small-signal model for synchronization stability of the GFL-VSC can be obtained, as shown in Fig. 3. This is similar to the classical Heffron-Phillips model of synchronous machines [4].

The synchronization stability mechanism of the GFL-VSC in a weak grid can be revealed by analyzing the manner in which Δu_{zq} introduces additional damping components to the equivalent model in the PLL.

$$\Delta u_{tq} = \underbrace{h_d(s)\Delta\delta_c}_{\Delta u_d} + \underbrace{h_q(s)\Delta\delta_c}_{\Delta u_q} + \underbrace{h_e(s)\Delta\delta_c}_{\Delta u_e} \tag{9}$$

The feedback loop shown in Fig. 3 consists of three parts, corresponding to the d-axis current loop $h_d(s)$, q-axis current loop $h_q(s)$, and grid voltage loop $h_e(s)$, respectively. In (9), under the interaction with $\Delta\delta_c$, the outputs of the three feedback loops (Δu_d, Δu_q, and Δu_e) collectively determine the damping characteristics of Δu_{tq}, which in turn affect system stability.

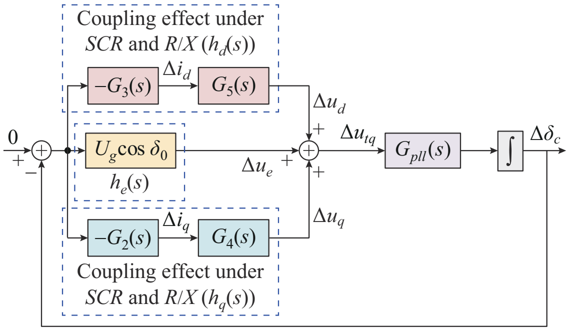

Fig. 3. Proposed small-signal model for synchronization stability of GFL-VSC.

III. Effect Mechanism of R/X on Synchronization Stability of GFL-VSC

A. Effects of R/X on Voltage Stability

A static analysis model can be obtained from (10). In inverter mode, $i_{d0}^*>0$, $i_{q0}^*<0$, and the maximum current injected into the grid is defined as $I_{\max}=1/L_g$, while ignoring filter parameters. When the grid impedance is not zero, i_q and R_g together form a positive damping effect ($h_q(s)$), which can offset the negative damping effect ($h_d(s)$) produced by i_d and L_g to a certain extent. However, the offset effect depends on the value of power output and grid impedance, that is, the sign of $R_g i_q^*+L_g i_d^*$.

$$u_{tq}=-U_g\sin\theta+R_g i_q^*+L_g i_d^* \tag{10}$$

where $\theta=\delta_c-\delta_g$.

When $\gamma=-i_d^*/i_q^*=\gamma_0$, $R_g i_q^*+L_g i_d^*=0$, and the system is in a steady state with $\theta=0$, the best synchronization stability is achieved. In this case, $\gamma=\gamma_0$ represents the optimal impedance ratio.

When $(I_{\max}\sin\theta-i_d^*)/i_q^*<\gamma<\gamma_0$, $R_g i_q^*+L_g i_d^*>0$, with $\theta>0$, $\gamma=(I_{\max}\sin\theta-i_d^*)/i_q^*$ is the lower limit value at which the system can maintain synchronization stability, denoted as γ_{ll}. The negative damping effect is strong, resulting in poor stability. However, we should note that if the output reactive power is increased, it can partially offset the negative damping effect caused by the active current and inductance, thereby enhancing the synchronization stability of the GFL-VSC.

When $\gamma_0<\gamma<-(I_{\max}\sin\theta+i_d^*)/i_q^*$, $R_g i_q^*+L_g i_d^*<0$, with $\theta<0$, $\gamma=-(I_{\max}\sin\theta+i_d^*)$ is the upper limit value at which the system can maintain synchronization stability, denoted as γ_{ul}. The positive damping effect dominates and completely offsets the negative damping effect. However, excessive reactive power output can cause the GFL-VSC to shift from positive to negative damping, thereby reducing the synchronization stability.

When $\gamma>\gamma_{ul}$ or $\gamma<\gamma_{ll}$, u_{tq} is always greater than or less than zero and the GFL-VSC does not have a steady-state equilibrium point, rendering it unable to maintain synchronization with the grid.

The stable range of R/X is denoted by $\gamma_{st}=\{\gamma|\gamma_{ll}<\gamma<\gamma_{ul}\}$. Within this range, the system exhibits a steady-state equilibrium point, and synchronization stability can be enhanced by introducing virtual impedance or adjusting the power reference values, as illustrated by the green region in Fig. 4(a). However, when R/X lies outside the set γ_{st}, denoted by $\complement_\gamma\gamma_{st}$, the system fails to maintain synchronization stability with the grid, as illustrated by the red region in Fig. 4(a). Here, $\complement_\gamma\gamma_{st}$ represents the complement of γ_{st}.

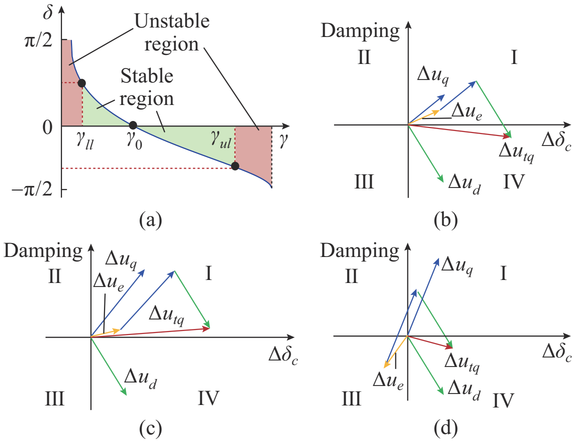

Fig. 4. Effects of γ on voltage stability. (a) Stability range of γ. (b) Negative damping with less γ. (c) Positive damping with suitable γ. (d) Negative damping with larger γ.

By combining (9), we can determine the system stability by the synthesized voltage. The voltages in quadrants I and II exhibit positive damping effects, whereas those in the remaining quadrants show negative damping effects. In Fig. 4(b), the synthesized voltage Δu_{tq} resides in quadrant IV, potentially triggering an oscillatory instability. Increasing either R/X or reactive power output, that is, increasing Δu_q, ensures the positioning of Δu_{tq} in quadrant I. This augmentation induces positive damping within the system, thereby reducing frequency oscillations and forcing the system to converge toward the equilibrium point, as shown in Fig. 4(c). Nevertheless, as depicted in Fig. 4(d), excessive values of R/X or reactive power output result in an undesirable shift from positive to negative damping effects during Δu_e. This shift causes Δu_{tq} to gravitate toward quadrant IV and leads to poor system stability.

Figure 5(a) illustrates the effects of R/X and SCR on u_{tq} in the static analysis, highlighting their significant influence on u_{tq}, particularly in a weak grid. These results underscore the close relationship between voltage stability and impedance. The corresponding sensitivity factor ε, depicted in Fig. 5(b), further substantiates this correlation. Specifically, when $SCR<3$ and $R/X<4.04$, $|\varepsilon|$ exhibits a larger magnitude. Furthermore, when R/X remains constant, an increase in SCR results in a decrease in $|\varepsilon|$. However, when R/X is equal to γ_0, $|\varepsilon|\approx 0$. This suggests that changes in grid strength have a negligible effect on voltage stability. Under a constant *SCR*, the influence of *R*/*X* on the voltage stability first decreases and then increases, and the influence is the smallest under the optimal impedance ratio.

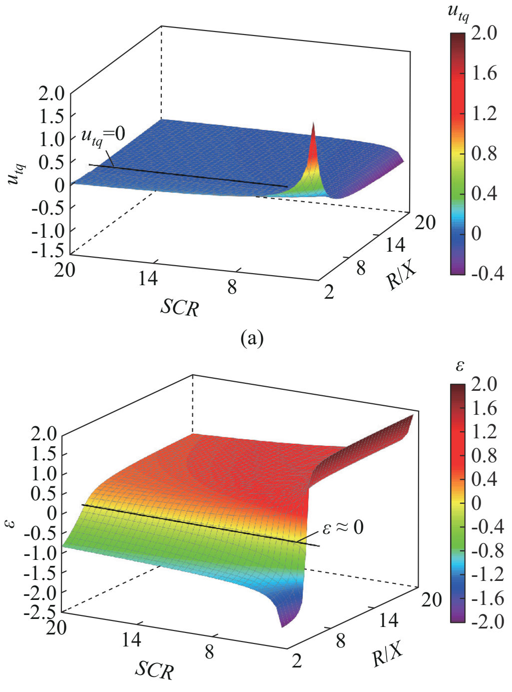

(a)

(b)

Fig. 5. Sensitivity analysis. (a) Effects of *R*/*X* and *SCR* on u_{tq}. (b) Sensitivity.

B. Effects of R/X on Power Angle Stability

As Fig. 3 shows, the internal relationship between Δu_{tq} and $\Delta\delta_c$ (Δu_{tq} divided by $\Delta\delta_c$) is defined as $G_E(s)$, and the relationship between $\Delta\delta_c$ and Δu_{tq} is defined as $G_F(s)$.

$$G_E(s)=\frac{\Delta u_{tq}}{\Delta\delta_c}=-(h_d(s)+h_e(s)+h_q(s)) \tag{11}$$

$$G_F(s)=\frac{\Delta\delta_c}{\Delta u_{tq}}=\frac{1}{s}G_{pll}(s) \tag{12}$$

To better illustrate the dynamic interaction between Δu_{tq} and $\Delta\delta_c$, the state variables at time i_{th} and $i_{th}+1$ are defined. For example, the state of Δu_{tq} at time i_{th} is denoted as $\Delta u_{tq,i}$, and therefore the state of $\Delta\delta_{c,i}$ at time i_{th} depends on $G_F(s)$ that is affected by the disturbance of $\Delta u_{tq,i}$. Then, $\Delta\delta_{c.i}$ affects Δu_{tq} by $G_E(s)$. Accordingly, the state of $\Delta\delta_c$ is eventually updated to $\Delta\delta_{c,i+1}$. Therefore, the convergence of the angle under small disturbances and the system stability can be described by the magnitude of $\Delta\delta_{c,i+1}/\Delta\delta_{c,i}$. The mathematical expression for the update behavior can be given as:

$$G_{EF}(s)=G_E(s)G_F(s)=\frac{\Delta u_{tq,i}}{\Delta\delta_{c,i}}\frac{\Delta\delta_{c,i+1}}{\Delta u_{tq,i}}=\frac{\Delta\delta_{c,i+1}}{\Delta\delta_{c,i}} \tag{13}$$

where $G_{EF}(s)$ is the convergence of the state variable $\Delta\delta_c$, and it evaluates the stable state of the system by participating in the dynamic feedback process. The stability margin depends on the infinite norm $\left\|G_{EF}(s)\right\|_\infty$, which represents the maximum value of $G_{EF}(s)$ under logarithmic amplitude-frequency characteristics. The smaller $\left\|G_{EF}(s)\right\|_\infty$ is, the larger is the stability margin. We can define λ as a feedback coefficient that reflects the amplitude relationship between $\Delta\delta_{c,i}$ and $\Delta\delta_{c,i+1}$ by:

$$\lambda=10^{\frac{\left\|G_{EF}(s)\right\|_\infty}{20}} \tag{14}$$

$$\Delta\delta_{c,i+1}=\lambda\Delta\delta_{c,i} \tag{15}$$

If $\left\|G_{EF}(s)\right\|_\infty>0$, $\lambda>1$. According to $\left|\Delta\delta_n\right|=\left|\lambda^n\right|\left|\Delta\delta_0\right|$, it can be obtained that $\lim\limits_{n\to\infty}\left|\Delta\delta_n\right|\to+\infty$. By contrast, for $\left\|G_{EF}(s)\right\|_\infty<0$, $0<\lambda<1$, and $\lim\limits_{n\to\infty}\left|\Delta\delta_n\right|\to 0$. Therefore, λ can be used as a criterion to assess synchronization stability. In other words, if $\lambda>1$, δ_c eventually diverges, leading to system destabilization. For $\lambda<1$, δ_c eventually converges to a steady-state value, resulting in progressive system stabilization.

Figure 6 shows a Bode diagram of $G_{EF}(s)$ under various conditions using the system parameters listed in Table I, where P^* and Q^* are the reference active power and reactive power of GFL-VSC, respectively.

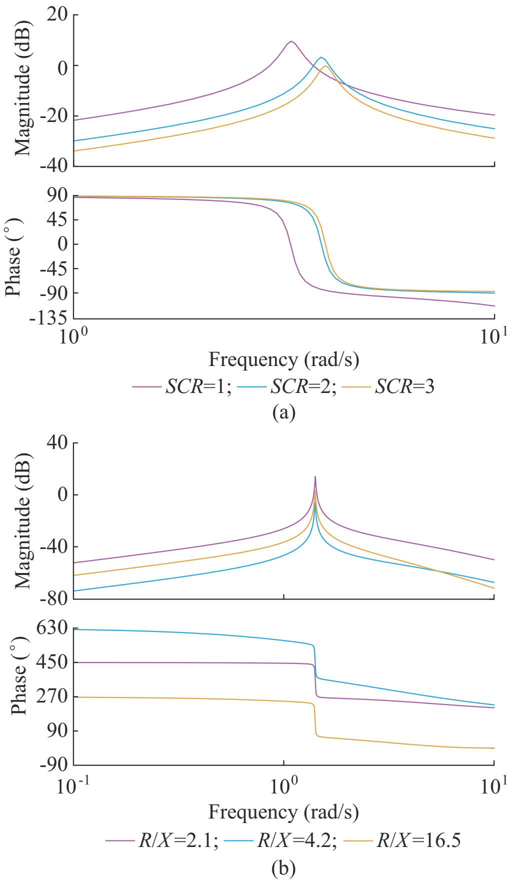

(a)

(b)

Fig. 6. Bode diagram of $G_{EF}(s)$ under various conditions. (a) $R/X=4.2$ and $SCR=1,2,3$. (b) $SCR=4.33$ and $R/X=2.1,4.2,16.5$.

In Fig. 6(a), as the amplitude of $G_{EF}(s)$ decreases, the phase margin gradually increases with an increase in the *SCR*, thereby weakening the negative damping characteristics.

TABLE I
SYSTEM PARAMETERS

Parameter	Value	Parameter	Value
U_g	1	Q^*	–0.24
ω_0	314	$k_{p,pll}$	0.2
R_f	0.01	$k_{i,pll}$	0.85
L_f	0.4	$k_{p,c}$	0.27
P^*	0.97	$k_{i,c}$	1

When $\lambda < 1$ and $SCR = 3$, the system will be affected by the positive damping, thereby enhancing the synchronization stability of the GFL-VSC. In addition, the theoretical analysis supports the practical observations in [4], confirming the validity of the established model and stability criterion.

The bode diagram presented in Fig. 6(b) shows the different results. With the increase of R/X, the amplitude of $G_{EF}(s)$ initially decreases to below zero, suggesting an augmentation of the positive damping traits in the system. However, as R/X continues to increase, the amplitude of $G_{EF}(s)$ exceeds zero again, triggering negative damping effects and compromising system stability. The resonant frequency remains relatively constant throughout this progression, whereas the phase margin experiences an initial decline, followed by an increase. Unlike the SCR, the effect of R/X on the system stability is non-monotonic, presenting a complex phenomenon. Hence, it is necessary to consider the effects of R/X on the project, rather than focusing only on SCR.

Figure 7 shows the root locus diagram of $G_{EF}(s)$ under various conditions. In the magnified diagram of the dominant pole in Fig. 7(a), the dominant pole clearly shifts from the positive to the negative half-plane with the increase of SCR. This movement enhances the system stability, reaching a stable state when $SCR = 3$. Notably, the eigenvalue analysis results are consistent with those obtained from the Bode diagram analysis.

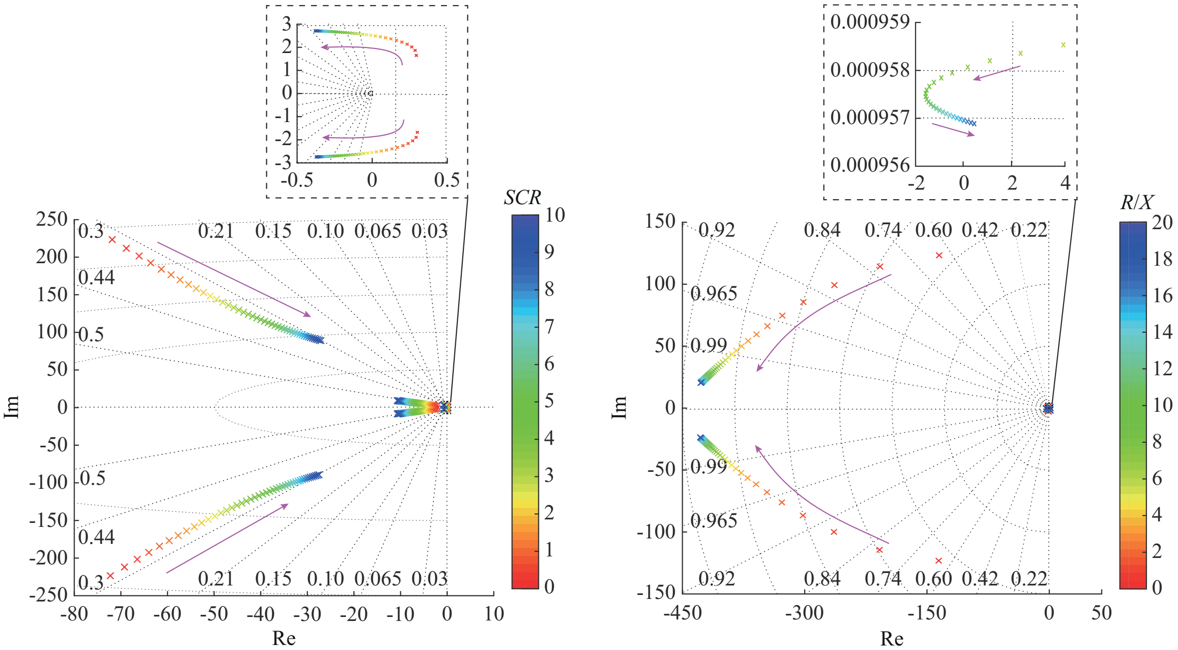

(a)

(b)

Fig. 7. Root locus diagram of $G_{EF}(s)$ under various conditions. (a) $R/X = 4.2$ and SCR in range of 1-3. (b) $SCR = 4.33$ and R/X in range of 0-20.

The root locus diagram presented as Fig. 7(b) illustrates the variation in R/X from 0 to 20 when $SCR = 4.33$. As R/X increases, the dominant pole crosses the imaginary axis and enters the positive half-plane, which gradually amplifies the negative damping effect. However, as R/X further increases, the positive damping effect diminishes, re-entering the positive half-plane when $\gamma = 16.0$ and leading to a loss of system stability. Thus, R/X affects the system stability by introducing a damping component; both excessively high and low R/X values can induce system synchronization instability. Only an appropriately selected R/X can foster synchronization stability. The root locus diagram illustrates the results of the theoretical analysis.

IV. SYNCHRONOUS VOLTAGE RECONSTRUCTION METHOD BASED ON GRID IMPEDANCE INFORMATION

In Fig. 8(a), $\dot{U}_t$ overlaps with the d axis, $u_{tq} = 0$, and the PLL successfully locks in phase. The angle between $\dot{U}_t$ and $\dot{U}_g$ is denoted as θ_1. However, as the grid strength diminishes, θ_1 changes as θ_2.

On the one hand, the increase in $\dot{U}_t$ causes θ_2 to advance the d axis during small disturbance dynamics, resulting in u_{tq} exceeding 0, as illustrated in Fig. 8(b). Consequently, the dq frame accelerates its rotation, signifying a continuous increase in ω_c. This acceleration may lead to the frame again overlapping with $\dot{U}_t$, significantly affecting the converter control loop based on the PLL dynamics and potentially causing instability. On the other hand, greater grid impedance requires a corresponding phase angle difference to effectively transmit active power, necessitating that $\dot{U}_t$ possesses a greater output phase angle. However, an excessively large phase angle can lead to stability issues.

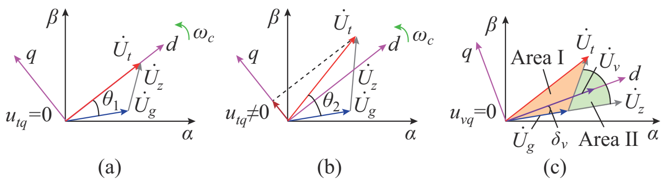

Fig. 8. Vector diagram under various conditions and principle of proposed method. (a) Under a steady-state condition. (b) Under small disturbance dynamics. (c) Principle of proposed method.

In summary, both the dynamic characteristic of the PLL and the static phase of the VSC synchronous voltage present significant challenges to system stability. Therefore, a synchronous voltage reconstruction method is proposed. Figure 9 presents a schematic of the proposed method.

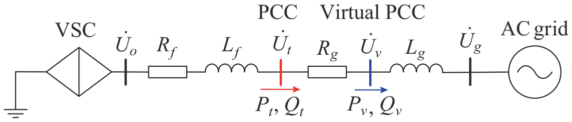

Fig. 9. Schematic of proposed method.

The classical method employs the phase angle of the PCC voltage to implement a GFL control algorithm. By contrast, the proposed method uses impedance information to reconstruct the virtual PCC, effectively reducing the impedance between $\dot{U}_t$ and $\dot{U}_g$, thus enhancing the stability of the GFL-VSC system. The virtual PCC is defined as:

$$\dot{U}_v=\dot{U}_t-(R_v+\mathrm{j}L_v)\dot{I}_{abc}=\dot{U}_t-(R_v+\mathrm{j}L_v)\frac{\dot{U}_o-\dot{U}_t}{R_f+\mathrm{j}L_f} \tag{16}$$

where $\dot{U}_v$ is the voltage of the virtual PCC; and R_v and L_v are the line impedances from the virtual PCC to the AC grid.

Based on this concept, the equation for calculating the reconstructed voltage of the virtual PCC is given in (17). The voltage of the virtual PCC can be constructed by controlling m and n, which can alter R/X and SCR. In other words, this method can change the position of the virtual PCC. The value ranges of m and n are [0, 1]. The larger the value, the closer it is to the power grid. Figure 8(c) shows that the manipulation of the scaling factors enables voltage adjustment of the impedance within area II, thereby impacting $\dot{U}_v$ in area I. δ_v is the angle of $\dot{U}_v$. As the values of m and n increase, the phase angle difference between $\dot{U}_t$ and $\dot{U}_g$ diminishes, thereby enhancing the system stability margin.

$$\begin{cases} u_{vd}=f[\gamma(m,n),S(m,n)]u_{td}-g[\gamma(m,n),S(m,n)]u_{od} \\ u_{vq}=f[\gamma(m,n),S(m,n)]u_{tq}-g[\gamma(m,n),S(m,n)]u_{oq} \end{cases} \tag{17}$$

$$\begin{cases} f[\gamma(m,n),S(m,n)]=1+\dfrac{m\gamma+\mathrm{j}n}{(R_f+\mathrm{j}L_f)\cdot SCR\cdot\sqrt{1+\gamma^2}} \\ g[\gamma(m,n),S(m,n)]=\dfrac{m\gamma+\mathrm{j}n}{(R_f+\mathrm{j}L_f)\cdot SCR\cdot\sqrt{1+\gamma^2}} \end{cases} \tag{18}$$

where $\gamma(m,n)$ and $S(m,n)$ are the functions of m and n; u_{vd} and u_{vq} are the reconstructed voltages of the virtual PCC in the dq frame; u_{od} and u_{oq} are the VSC output voltages in the dq frame; and m and n are the scale factors of the grid resistance and inductance, respectively.

Compared with traditional methods, the proposed method reconstructs the SCR and R/X by changing the values of the scaling factors. This allows the controller to improve its dynamic characteristics more smoothly under varying grid conditions.

Notably, the proposed method relies on impedance information from (16). The equivalent grid impedance observed from the converter may not always be accurately known and may change with the reconfiguration of the grid. Therefore, achieving complete compensation for the grid impedance may not be practical. However, it is asserted that even partial impedance compensation can enhance the stability range without adversely affecting converter operation. Thus, the grid impedance can be estimated based on the type and length of the transmission line during practical operation. The impedance amplification factor can be appropriately adjusted to more closely reflect the actual grid impedance, depending on grid conditions. In addition, the proposed method can be combined with remote measurements of active and reactive power flows to facilitate impedance estimation, as indicated in [28] and [29].

V. EXPERIMENTAL RESULTS

To validate the correctness and effectiveness of the theoretical analysis and proposed method, a hardware-in-the-loop (HIL) platform was constructed using the TMS320F28377D device, as illustrated in Fig. 10, with the experimental parameters and cases listed in Tables I and II, respectively.

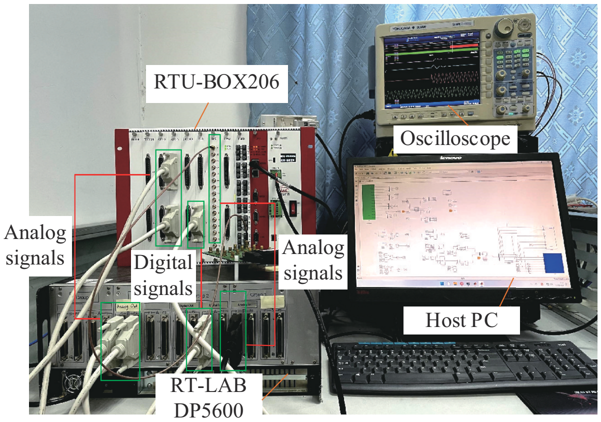

Fig. 10. HIL platform.

A. Grid Strength from Strong to Weak

The synchronization characteristics of the GFL-VSC system in Case 1 are illustrated in Fig. 11(a). The blue dashed line represents the switching of the line condition in related case. The yellow, gray, and blue colors of the U_t curves represent the voltages of phases A, B, and C, respectively. The red, orange, and blue colors of the I_{abc} curves represent the currents of phases A, B, and C, respectively.

TABLE II
LINE PARAMETERS UNDER DIFFERENT CASES BEFORE AND AFTER SWITCHING OF LINE CONDITION

Case	Before		After	
	SCR	*R*/*X*	*SCR*	*R*/*X*
Case 1	4.33	4.20	2.04	4.20
Case 2	4.33	4.20	4.33	0.50
Case 3	2.50	4.20	1.50	4.20
Case 4	4.33	0.50		
Case 5	1.50	14.98		
Case 6	4.33	2.01	2.04 (GFL-VSC$_1$) 1.50 (GFL-VSC$_2$)	2.01 (GFL-VSC$_1$) 0.50 (GFL-VSC$_2$)

The related curves in the other figures below have similar meanings and will not be repeated. When the grid strength abruptly shifts from strong to weak, the power, voltage, and current of the GFL-VSC system are affected, resulting in a loss of synchronization with the grid. However, applying the proposed method yields improved synchronization stability, as indicated by the experimental results presented in Fig. 12. Figure 12(a) shows that P_t and Q_t at the PCC are re-established to be stable and slightly higher than the rated values after a short adjustment period, which is attributed to the reconstructed voltage being closer to the grid side. To achieve the rated values of power P_v and Q_v at the virtual PCC, a greater output power at the PCC is required to offset the consumption on the line, as shown in Fig. 12(b). Overall, the experimental results demonstrate the effectiveness of the proposed method under weak grid conditions.

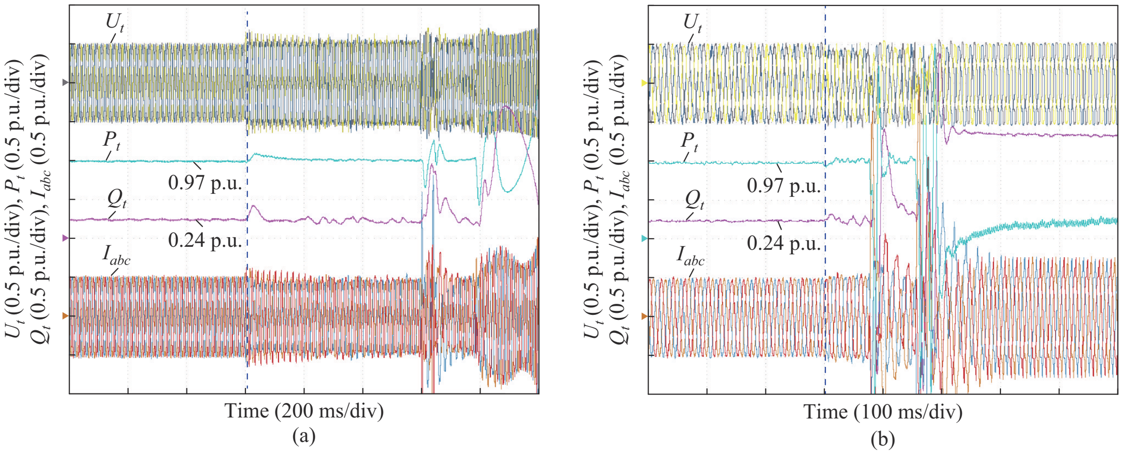

(a) (b)

Fig. 11. Experimental results at PCC without proposed method. (a) Case 1. (b) Case 2.

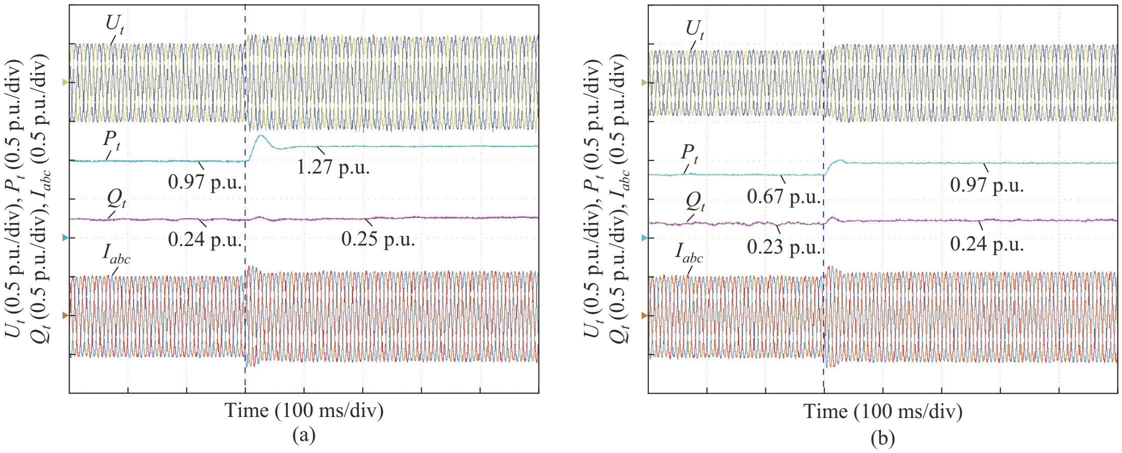

(a) (b)

Fig. 12. Experimental results of Case 1 with proposed method. (a) PCC. (b) Virtual PCC.

B. R/X Transition from Appropriate to Small

Experimental results of Case 2 are shown in Fig. 11(b). Clearly, the system stability deteriorates as R/X changes from 4.2 to 0.5. The loss of synchronization observed is attributed to the excessively small R/X, which is consistent with the theoretical analysis. Figure 13 presents the experimental results after implementing the proposed method, which demonstrates that the proposed method effectively alters R/X, thereby enhancing the synchronization stability.

C. Comparison Under Extremely Weak Grid Conditions

Figure 14 presents the experimental results of Case 3 with both the virtual inductance method in [20] and the proposed method. Both methods are stabilized under a weak grid condition with $SCR = 2.5$. However, the proposed method achieves a slightly higher power at the PCC compared with the virtual inductance method, as it adequately meets the power requirements at the virtual PCC, thus compensating for power at the PCC.

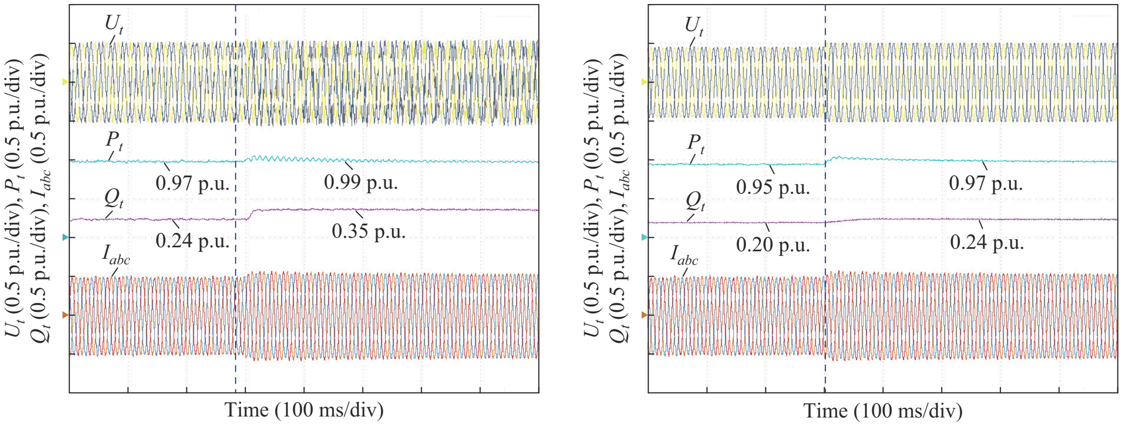

(a) (b)

Fig. 13. Experimental results of Case 2 with proposed method. (a) PCC. (b) Virtual PCC.

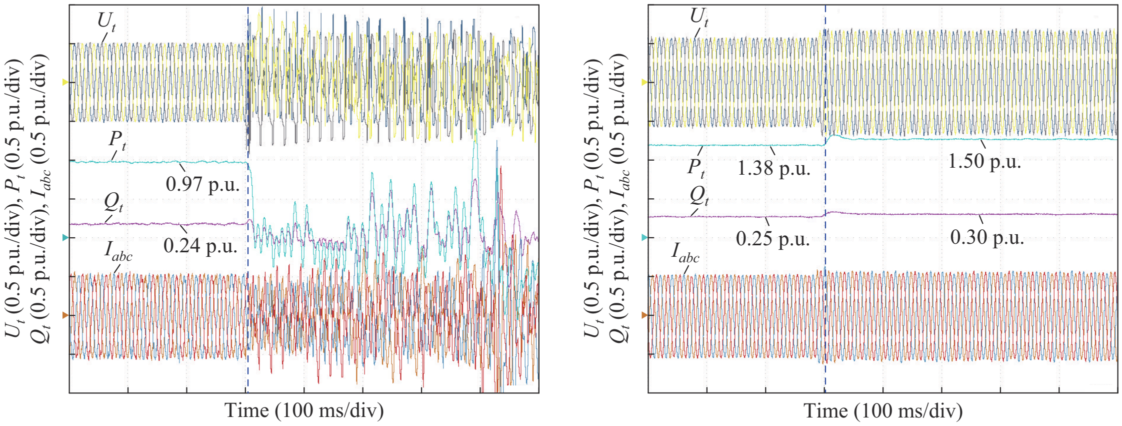

(a) (b)

Fig. 14. Experimental results of Case 3 with various methods. (a) Method in [20]. (b) Proposed method.

In addition, when $SCR=1.5$, the virtual inductance method loses stability, whereas the proposed method maintains stability, as shown in Fig. 14(b). These results indicate that the proposed method can operate stably not only under $SCR<3$ (weak grid) but also under $SCR<2$ (extremely weak grid [16]).

D. Influence of Reference Power on Synchronization Stability

In Case 4, P^* and Q^* mutate from 0.97 to 1.97 and from 0.1 to 0.24, respectively. The experimental results are shown in Fig. 15(a) and (b). Although the system operates in a strong grid, R/X is close to γ_{ll}, resulting in poor stability. A sudden increase in P^* enhances the negative damping effect and reduces the system stability. By contrast, a sudden increase in Q^* enhances the positive damping effect and improves the system stability. Nevertheless, in Case 5, as shown in Fig. 15(c), the system operates under extremely weak grid conditions with R/X closer to γ_{ul}. In addition, the positive damping effect dominates, allowing the system to maintain its stability. However, a sudden change in Q^* can reverse the positive damping effect a negative one, resulting in system instability.

The comparison of Cases 4 and 5 reveals that: ① a smaller R/X under strong grid conditions can worsen system stability, whereas the system can achieve stability under weak grid conditions at equilibrium with an appropriately high R/X; ② increasing Q^* can enhance system stability within a certain R/X range, but this effect will be counterproductive at high R/X values.

Figure 15(d) presents the experimental results of Case 5 with the proposed method. After an adjustment period of 100 ms, the system returns to a steady-state equilibrium point. This demonstrates that the proposed method effectively mitigates the negative impact of reactive power by modifying R/X.

E. Verification of Proposed Method for Multiple VSCs

Based on the topology shown in Fig. 16, the working condition shown in Case 6 is verified. P_{ti} and Q_{ti} are the active and reactive power outputs of GFL-VSC$_i$, respectively, with a ratio of $P_{t1}:P_{t2}=1:2$ and $Q_{t1}:Q_{t2}=1:2$. L_{gi} and R_{gi} are the grid inductance and resistance of GFL-VSC$_i$, respectively. U_{ti} is the voltage output of GFL-VSC$_i$. In the absence of any additional control, GFL-VSC$_1$ and GFL-VSC$_2$ are unstable to varying degrees in the face of grid impedance changes, as shown in Fig. 17(a). Experimental results obtained after applying the proposed method are shown in Fig. 17(b). Both GFL-VSC$_1$ and GFL-VSC$_2$ demonstrate stable and proportional output, confirming the feasibility of applying the proposed method to multiple VSCs.

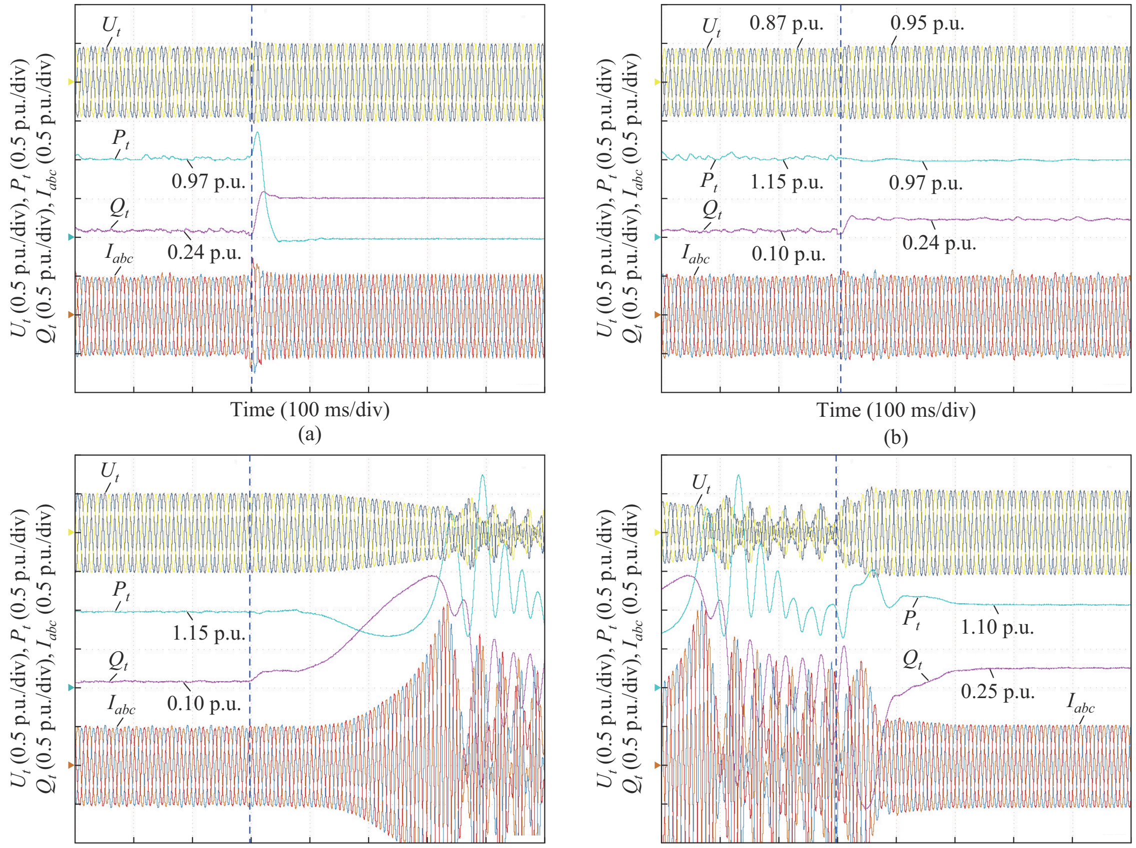

(a) (b) (c) (d)

Fig. 15. Experimental results of Cases 4 and 5. (a) Case 4: P^* from 0.97 to 1.97. (b) Case 4: Q^* from 0.1 to 0.24. (c) Case 5: Q^* from 0.1 to 0.24. (d) Case 5 with proposed method.

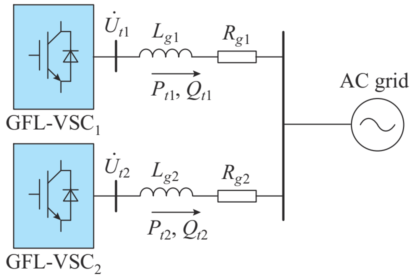

Fig. 16. Topology of Case 6.

VI. CONCLUSION

Grid impedance negatively affects the synchronization stability of GFL-VSC, and this effect cannot be overlooked. This study aimed to explore the underlying mechanisms and proposed an improved method. First, a small-signal model of GFL-VSC was established to describe the complex dynamic coupling process between the grid impedance and the control loop. Next, the effect of R/X on voltage and power angle stability was analyzed, where its effect on system damping was clarified from a physical perspective.

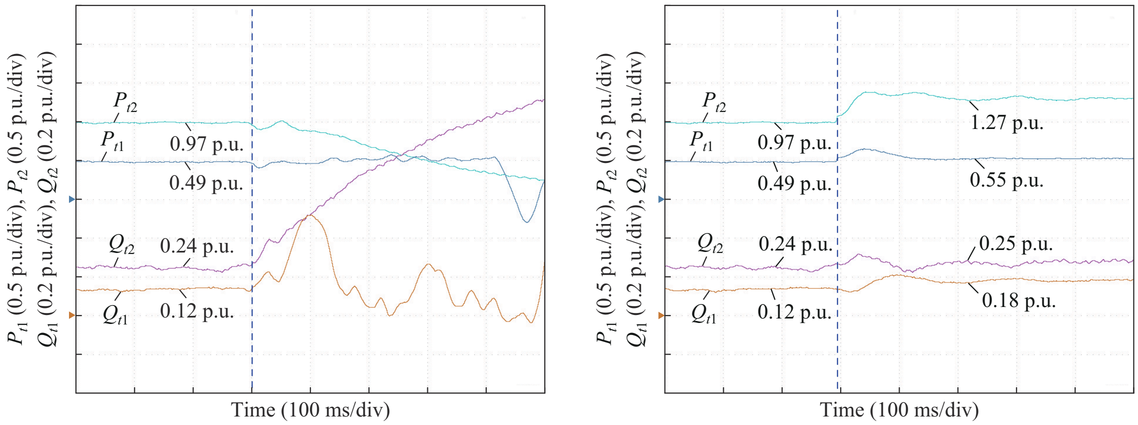

(a) (b)

Fig. 17. Experimental results of Case 6. (a) Without proposed method. (b) With proposed method.

Based on this analysis, the stability range of R/X was quantified, and a power angle stability criterion was proposed. In addition, a synchronous voltage reconstruction method was proposed to enhance the synchronization stability of the system by altering *SCR* and R/X. This method did not rely on the transformation of the PLL itself and demonstrated good adaptability across various power grid strengths and multi-machine parallel connections. Finally, experimental results validated the accuracy and effectiveness of both the analytical analysis and proposed method.

REFERENCES

[1] Z. Zhou, Z. Chen, X. Wang *et al*., "AC fault ride through control strategy on inverter side of hybrid HVDC transmission systems," *Journal of Modern Power Systems and Clean Energy*, vol. 7, no. 5, pp. 1129-1141, Sept. 2019.

[2] Y. Wang, F. Qiu, G. Liu *et al*., "Adaptive reference power based voltage droop control for VSC-MTDC systems," *Journal of Modern Power Systems and Clean Energy*, vol. 11, no. 1, pp. 381-388, Jan. 2023.

[3] Q. Jia, G. Yan, Y. Cai *et al*., "Small-signal stability analysis of photovoltaic generation connected to weak AC grid," *Journal of Modern Power Systems and Clean Energy*, vol. 7, no. 2, pp. 254-267, Mar. 2019.

[4] S. Tan, H. Geng, and G. Yang, "Phillips-Heffron model for current-controlled power electronic generation unit," *Journal of Modern Power Systems and Clean Energy*, vol. 6, no. 3, pp. 582-594, May 2018.

[5] J. Zhou, H. Ding, S. Fan *et al*., "Impact of short-circuit ratio and phase-locked-loop parameters on the small-signal behavior of a VSC-HVDC converter," *IEEE Transactions on Power Delivery*, vol. 29, no. 5, pp. 2287-2296, Oct. 2014.

[6] T. Magg, M. Manchen, E. Krige *et al*., "Connecting networks with VSC HVDC in Africa: Caprivi link interconnector," in *Proceedings of IEEE PES Conference and Exposition in Africa*: *Intelligent Grid Integration of Renewable Energy Resources*, Johannesburg, South Africa, Jul. 2012, pp. 1-6.

[7] R. Yin, Y. Sun, S. Wang *et al*., "Stability analysis of the grid-tied VSC considering the influence of short circuit ratio and *X*/*R*," *IEEE Transactions on Circuits and Systems II*: *Express Briefs*, vol. 69, no. 1, pp. 129-133, Jan. 2022.

[8] G. Li, Y. Chen, A. Luo *et al*., "An enhancing grid stiffness control strategy of STATCOM/BESS for damping sub-synchronous resonance in wind farm connected to weak grid," *IEEE Transactions on Industrial Informatics*, vol. 16, no. 9, pp. 5835-5845, Sept. 2020.

[9] J. Z. Zhou and A. M. Gole, "VSC transmission limitations imposed by AC system strength and AC impedance characteristics" in *Proceedings of 10th IET International Conference on AC and DC Power Transmission*, Birmingham, UK, Dec. 2012, pp. 1-6.

[10] R. Pan, D. Liu, S. Liu *et al*., "Stability comparison between grid-forming and grid-following based wind farms integrated MMC-HVDC," *Journal of Modern Power Systems and Clean Energy*, vol. 11, no. 4, pp. 1341-1355, Jul. 2023.

[11] A. Kuri, R. Zurowski, G. Mehlmann *et al*., "A novel grid forming control scheme revealing a true inertia principle," *IEEE Transactions on Power Systems*, vol. 36, no. 6, pp. 5369-5384, Nov. 2021.

[12] M. Chen, D. Zhou, and F. Blaabjerg, "Modelling, implementation, and assessment of virtual synchronous generator in power systems," *Journal of Modern Power Systems and Clean Energy*, vol. 8, no. 3, pp. 399-411, May 2020.

[13] K. Sun, W. Yao, J. Wen *et al*., "A two-stage simultaneous control scheme for the transient angle stability of VSG considering current limitation and voltage support," *IEEE Transactions on Power Systems*, vol. 37, no. 3, pp. 2137-2150, May 2022.

[14] L. Dewangan and H. J. Bahirat, "Controller interaction and stability margins in mixed SCR MMC-based HVDC grid," *IEEE Transactions on Power Systems*, vol. 35, no. 4, pp. 2835-2846, Jul. 2020.

[15] C. Li, W. Liu, J. Liang *et al*., "Improved grid impedance compensation for phase-locked loop to stabilize the very-weak-grid connection of VSIs," *IEEE Transactions on Power Delivery*, vol. 37, no. 5, pp. 3863-3872, Oct. 2022.

[16] Z. Shuai, Y. Li, W. Wu *et al*., "Divided DQ small-signal model: a new perspective for the stability analysis of three-phase grid-tied inverters," *IEEE Transactions on Industrial Electronics*, vol. 66, no. 8, pp. 6493-6504, Aug. 2019.

[17] H. Zhang, L. Harnefors, X. Wang *et al*., "Stability analysis of grid-connected voltage-source converters using SISO modeling," *IEEE Transactions on Power Electronics*, vol. 34, no. 8, pp. 8104-8117, Aug. 2019.

[18] J. Fang, X. Li, X. Yang *et al*., "An integrated trap-LCL filter with reduced current harmonics for grid-connected converters under weak grid conditions," *IEEE Transactions on Power Electronics*, vol. 32, no. 11, pp. 8446-8457, Nov. 2017.

[19] X. Li, J. Fang, Y. Tang *et al*., "Capacitor-voltage feedforward with full delay compensation to improve weak grids adaptability of LCL-filtered grid-connected converters for distributed generation systems," *IEEE Transactions on Power Electronics*, vol. 33, no. 1, pp. 749-764, Jan. 2018.

[20] A. Adib and B. Mirafzal, "Virtual inductance for stable operation of grid-interactive voltage source inverters," *IEEE Transactions on Industrial Electronics*, vol. 66, no. 8, pp. 6002-6011, Aug. 2019.

[21] X. Zhang, D. Xia, Z. Fu *et al*., "An improved feedforward control method considering PLL dynamics to improve weak grid stability of grid-connected inverters," *IEEE Transactions on Industry Applications*, vol. 54, no. 5, pp. 5143-5151, Sept. 2018.

[22] Z. Xie, Y. Chen, W. Wu *et al*., "Stability enhancing voltage feed-forward inverter control method to reduce the effects of phase-locked loop and grid impedance," *IEEE Journal of Emerging and Selected Topics in Power Electronics*, vol. 9, no. 3, pp. 3000-3009, Jun. 2021.

[23] J. Khazaei, M. Beza, and M. Bongiorno, "Impedance analysis of modular multi-level converters connected to weak AC grids," *IEEE Transactions on Power Systems*, vol. 33, no. 4, pp. 4015-4025, Jul. 2018.

[24] M. F. M. Arani and Y. A. R I. Mohamed, "Analysis and performance enhancement of vector-controlled VSC in HVDC links connected to very weak grids," *IEEE Transactions on Power Systems*, vol. 32, no. 1, pp. 684-693, Jan. 2017.

[25] M. Berg, A. Aapro, R. Luhtala *et al*., "Small-signal analysis of photovoltaic inverter with impedance-compensated phase-locked loop in weak grid," *IEEE Transactions on Energy Conversion*, vol. 35, no. 1, pp. 347-355, Mar. 2020.

[26] P. Sun, J. Yao, R. Liu *et al*., "Virtual capacitance control for improving dynamic stability of the DFIG-based wind turbines during a symmetrical fault in a weak AC grid," *IEEE Transactions on Industrial Electronics*, vol. 68, no. 1, pp. 333-346, Jan. 2021.

[27] O. Abdoli, M. Gholipour, and R. A. Hooshmand, "Improving synchronization stability of grid connected converters by virtual impedance," *IET Generation*, *Transmission & Distribution*, vol. 15, no. 7, pp. 1136-1143, Apr. 2021.

[28] N. Mohammed, M. H. Ravanji, W. Zhou *et al*., "Online grid impedance estimation-based adaptive control of virtual synchronous generators considering strong and weak grid conditions," *IEEE Transactions on Sustainable Energy*, vol. 14, no. 1, pp. 673-687, Jan. 2023.

[29] D. K. Alves, R. L. A. Ribeiro, F. B. Costa *et al*., "Real-time wavelet-based grid impedance estimation method," *IEEE Transactions on Industrial Electronics*, vol. 66, no. 10, pp. 8263-8265, Oct. 2019.

Weiye Diao received the M.S. degree in power system and automation from Hunan University of Technology, Zhuzhou, China, in 2022. He is currently working toward the Ph.D. degree in electrical engineering with Southeast University, Nanjing, China. His research interests include renewable energy power conversion and grid connection technology, AC/DC microgrid control technology, and high-voltage direct current (HVDC).

Ao Liu received the bachelor's degree in electrical engineering from Shanxi University of Science and Technology, Xi'an, China, in 2022. He is currently pursuing the master's degree in electrical engineering with Southeast University, Nanjing, China. His research interests include modular multilevel converter based high-voltage direct current (MMC-HVDC) and power grid stability.

Jun Mei received the B.S. degree in radio engineering from Chongqing University, Chongqing, China, in 1994, and the M.S. and Ph.D. degrees in electrical engineering from Southeast University, Nanjing, China, in 2001 and 2006, respectively. From 2011 to 2012, he was a Visiting Scholar at The University of Tennessee, Knoxville, USA. He is currently an Associate Professor with the School of Electrical Engineering, Southeast University. His research interests include electric power converter for distributed energy source, flexible alternative current transmission system (FACTS), HVDC, and power quality control.

Linyuan Wang received the B.S. degree in electronic engineering from the Southeast University, Nanjing, China, in 2022. He is currently pursuing the M. S. degree in electronic engineering with Southeast University, Nanjing, China. His research interests include MMC-HVDC and power grid stability.

Guanghua Wang received the M. S. degree in electrical engineering from Nanjing Normal University, Nanjing, China, in 2022. He is currently pursuing the Ph. D. degree in electrical engineering with Southeast University, Nanjing, China. His research interest includes planning of distributed generation.

Fujin Deng received the B. S. degree in electrical engineering from China University of Mining and Technology, Jiangsu, China, in 2005, the M.S. degree in electrical engineering from Shanghai Jiao Tong University, Shanghai, China, in 2008, and the Ph.D. degree in energy technology from the Department of Energy Technology, Aalborg University, Aalborg, Denmark, in 2012. His main research interests include wind power generation, multilevel converter, HVDC technology, DC grid, and power system dynamics with offshore wind farm.